In Situ STEM Study on the Morphological Evolution of Copper-Based Nanoparticles During High Temperature Redox Reactions

Sharmin Sharna, Mounib Bahri, Corinne Bouillet, Virgile Rouchon, Arnold Lambert, Anne-Sophie Gay, David Chiche, Ovidiu Ersen

▶ **To cite this version:**

Sharmin Sharna, Mounib Bahri, Corinne Bouillet, Virgile Rouchon, Arnold Lambert, et al.. In Situ STEM Study on the Morphological Evolution of Copper-Based Nanoparticles During High Temperature Redox Reactions. Nanoscale, 2021, 13 (21), pp.9747-9756. 10.1039/D1NR01648B . hal-03288747

HAL Id: hal-03288747
https://ifp.hal.science/hal-03288747

Submitted on 16 Jul 2021

HAL is a multi-disciplinary open access archive for the deposit and dissemination of scientific research documents, whether they are published or not. The documents may come from teaching and research institutions in France or abroad, or from public or private research centers.

L'archive ouverte pluridisciplinaire **HAL**, est destinée au dépôt et à la diffusion de documents scientifiques de niveau recherche, publiés ou non, émanant des établissements d'enseignement et de recherche français ou étrangers, des laboratoires publics ou privés.

In-situ STEM study on the morphological evolution of copper-based nanoparticles during high-temperature redox reactions

Sharmin Sharna [a, b], Mounib Bahri [b], Corinne Bouillet [b], Virgile Rouchon [a], Arnold Lambert [a], Anne-Sophie Gay [a], David Chiche [a] and Ovidiu Ersen [*b]

Despite the broad relevance of copper nanoparticles in industrial applications, the fundamental understanding of oxidation and reduction of copper at the nanoscale is still a matter of debate and remains within the realm of bulk or thin film-based systems. Moreover, the reported studies on nanoparticles vary widely in terms of experimental parameters and are predominantly carried out using either ex-situ observation or environmental transmission electron microscopy in a gaseous atmosphere at low pressure. Hence, dedicated studies in regards to the morphological transformations and structural transitions of copper-based nanoparticles at a wider range of temperatures and under industrially relevant pressure would provide valuable insights to improve the application-specific material design. In this paper, copper nanoparticles are studied using in-situ Scanning Transmission Electron Microscopy to discern the transformation of the nanoparticles induced by oxidative and reductive environments at high temperatures. The nanoparticles were subjected to a temperature of 150 °C to 900 °C at 0.5 atm partial pressure of the reactive gas, which resulted in different modes of copper mobility both within the individual nanoparticles and on the surface of the support. Oxidation at an incremental temperature revealed the dependency of the nanoparticles' morphological evolution on their initial size as well as reaction temperature. After the formation of an initial thin layer of oxide, the nanoparticles evolved to form hollow oxide shells. The kinetics of formation of hollow particles were simulated using a reaction-diffusion model to determine the activation energy of diffusion and temperature-dependent diffusion coefficient of copper in copper oxide. Upon further temperature increase, the hollow shell collapsed to form compact and facetted nanoparticles. Reduction of copper oxide was carried out at different temperatures starting from various oxide phase morphologies. A reduction mechanism is proposed based on the dynamic of the reduction-induced fragmentation of the oxide phase. In a broader perspective, this study offers insights into the mobility of the copper phase during its oxidation-reduction process in terms of microstructural evolution as a function of nanoparticle size, reaction gas, and temperature.

Introduction

Copper nanoparticles (NPs) in both metallic and oxide forms are widely utilized in industrial applications ranging from technological use as interconnects [1] to photovoltaics [2] and sensors [3], as well as in heterogeneous catalysis [4] such as Water-Gas-Shift reaction (WGS) [5], methanol synthesis[6], CO oxidation [7] and selective catalytic conversion of NO_x [8]. Recently, copper-based nanoparticles have received renewed interest as oxygen carrier (OC) in Chemical Looping Combustion (CLC), an alternative combustion process with low energy penalty carbon dioxide capture solution [9]. CLC can be performed using a supported copper-based OC that undergoes successive reduction (combustion of hydrocarbon) and oxidation (regeneration of the oxide phase) cycles to produce energy; this approach eliminates direct contact between the

[a.] *IFP Energies Nouvelles, Rond-Point de l'échangeur de Solaize, 69360 Solaize, France*
[b.] *Institute de Physique et Chimie des Matériaux de Strasbourg (IPCMS), UMR 7504 CNRS – Université de Strasbourg, 23 rue du Loess, BP 43, Strasbourg Cedex 2, France*
*Email: ovidiu.ersen@ipcms.unistra.fr

air and the fuel and allows the generation of a readily separable stream of CO_2 [10]. Depending on the application, copper-based NPs are subjected to different oxidizing/reducing environments at variable pressures and temperatures ranging from 200-300 °C in WGS to above 800-1000 °C in CLC application [5,9,10]. The exposure of Cu-based NPs to different reaction conditions leads to chemical, structural and morphological transformations in the material resulting in oxidation [11], reduction [10], and sintering [12] of the copper phases, causing degradation in their reactivity and selectivity. Although a wealth of literature is available depicting the oxidation-reduction mechanisms of copper, variable experimental conditions give rise to discrepancies in the observations, making it difficult to unravel the contribution of different experimental parameters such as NP size, temperature, type, and pressure of gas and metal-support interactions [12,12–16]. Thus, understanding the oxidation mechanism of copper NPs and their subsequent reduction under reaction conditions is of special interest to not only optimize oxygen carrier design but also to stabilize specific copper phases for other applications.

A significant amount of research has been dedicated to the comprehension of copper oxidation, but much of it remains within the domain of thin films [17]. However, several works on the oxidation of copper nanoparticles were also carried out using either transmission electron microscopy (TEM) to understand the effect of temperature on the morphology of the oxide phase [15,18,19], thermogravimetric analysis (TGA) to study the kinetics of oxidation [16,20], environmental scanning TEM (e-STEM) to directly visualize the dynamic evolution of the nanoparticle morphology [21], or real-time surface plasmon spectroscopy [13,14]. The oxidation of copper nanoparticles is affected by the reaction conditions as well as the microstructure of the starting metallic phase leading to a final morphology of the oxide nanoparticles which is determined by the temperature of oxidation. Typically, at intermediate temperatures (50-300 °C), for a NP size distribution of 10-30 nm diameter, the oxidation can be considered as a two-steps process: the initial step involves the formation of a thin layer of Cu_2O oxide encapsulating the metallic copper core, followed by the genesis of hollow nanoparticles related to outward growth of oxide, due to differential diffusion of the reaction species via Nanoscale Kirkendall Effect (NKE), at 0.21 atm O_2 partial pressure [13,15,16,18,22–24]. In contrast, LaGrow et al. have reported layer-by-layer growth of compact oxide nanoparticles from a single nucleation point of the metallic copper at 300-500 °C under a very low O_2 partial pressure (2×10^{-5} - 10^{-4} atm) [21]. Regarding the phase changes throughout oxidation, Nakamura et al. reported a phase transition from Cu_2O to CuO above a temperature of 300 °C at 0.21 atm O_2 partial pressure, while LaGrow et al. reported the presence of Cu_2O phase only, up to a temperature of 500 °C [15,21]. The oxygen partial pressure is hence an important parameter affecting the oxidation mechanism that requires further investigation. Indeed, according to Haugsrud and Kofstad, depending on the O_2 partial pressure, the oxidation of Cu proceeds either via singly charged copper vacancy at low pressure or via neutral copper vacancy at higher pressure, consequently affecting the mechanism of oxidation [25]. Upon further increase in temperature, the hollow NPs are subjected to collapse and formation of compact NPs, as demonstrated by Nakamura et al. [15] and Rice et al [14].

Not many studies can be found in the literature for the reduction of copper oxide NPs. Recently, the morphological transformation during Cu_2O reduction has been discerned by in-situ STEM at 300-500 °C under 2×10^{-5} - 10^{-4} atm H_2 partial pressure. The reduction of Cu_2O to Cu NPs occurred from a single nucleation site on the surface of the copper oxide where the reaction front moved unidirectionally with time [21]. In comparison, other transition metal-oxide NPs such as oxides of Ni or Co undergo NP re-dispersion via fragmentation during the reduction reactions [26,27]. The difference in the observations could stem from the shape and microstructure of the initial oxide NPs or the reaction conditions, such as H_2 partial pressure. Particle morphology and H_2 partial pressure also have an impact on the kinetics of reduction as demonstrated by Kim et al. [28] and Rodriguez et al. [29]. It was suggested that an increase in the particles' structural defect concentration and H_2 partial pressure induces faster nucleation, and a faster rate of metallic copper formation was observed.

Notwithstanding the number of studies conducted on copper, numerous open questions remain, including how the dynamic shape evolution proceeds during oxidation under high O_2 partial pressure, or the assessment of the reduction

mechanism of copper oxide NPs. In this context, our general goal is to investigate, by directly monitoring the various phenomena involved in the oxidation and reduction processes of copper NPs, by systematically varying the temperature of the reaction and quantifying the structural changes induced in the NPs. Herein, we report the dynamic chemical, structural, and morphological transformation of copper phases using in-situ Scanning Transmission Electron Microscopy (STEM). Notably, the in-situ setup operates at atmospheric pressure to approach the industrial operating conditions.

Experimental

Materials and Methods

Nanoparticle synthesis: In the present study, two types of NPs preparation were used: Cu NPs produced via sputtering and by chemical synthesis route.

The sputtered samples were prepared by magnetron sputtering of copper from a copper target using DP650 sputtering equipment (from Alliance Concept) by directly sputtering 1-2 nm thickness of Cu thin-film at 150 mA onto the amorphous SiN_x MEMS chip (from Protochips). The assembled SiN_x e-chip was then inserted in the TEM for in-situ heat treatment at 300 °C under 0.5 atm H_2 partial pressure to produce oxide-free metallic copper NPs. Three experiments were conducted to achieve different particle size distributions (PSD) by varying either the thickness of the film or the rate of heating during the NPs formation step. The details of the preparation steps and the resulting PSD are presented in Supporting Information (SI - 1.1). The samples are called Sputt-1 (bimodal PSD of 4 ± 2 nm and 35 ± 7 nm), Sputt-2 (bimodal PSD of 4 ± 2 nm and 21 ± 6 nm) and Sputt-3 (monomodal PSD 9 ± 4 nm).

The second type of sample was produced via a chemical route adapted from Carenco et al. by thermally reducing copper acetate in the presence of oleylamine and octadecene [30]. Typically, 25.1 mL (10 parts) of oleylamine was added together with 10 mL of octadecene in a 100 mL round bottom flask, followed by 1.53 g (1 part) of copper acetate, then stirred at 50 °C. The mixture was then heated to 250 °C in a sand bath for 2 hours until the mixture turned reddish black. The resulting nanoparticles were isolated using centrifugation in a mixture of methanol/n-hexane/acetone in a 1:2:10 ratio and finally suspended in a solution of hexane. For the in-situ STEM observation, a few drops of the sample dispersed in hexane were deposited on the SiN_x membrane and dried. The colloidal nanoparticles were heated under Ar at 200 °C for 2.5 hours, followed by a reduction reaction under 0.5 atm H_2 at 500°C for 1 hour to ensure the removal of the organic surfactants and presence of metallic NPs (Figure S2 in SI) [31]. This sample is referred to as Syn-1 (with a bimodal PSD of 17 ± 5 nm and 42 ± 6 nm) after heat treatment (Figure 1). The NPs were imaged by HR-STEM under Argon after synthesis and under H_2 after heat treatment at 500 °C (Figure S2 and S3).

In-situ STEM: The experiments were carried out using a JEOL JEM-2100F microscope operated at 200 kV equipped with a spherical aberration probe corrector (Cs from CEOS), high-resolution objective lens pole piece and an UltraScan 1000 CCD array detector (GATAN). For in-situ observations, a Protochips Atmosphere system was used [32]. The samples were suspended between two micro-electro-mechanical systems (MEMS) based closed cells made up of transparent SiN_x (for observation) and SiC (for heating) [33,34]. The in-situ observations were carried out at a pressure of 1 atm (10^5 Pa) and a temperature of up to 900 °C under oxidative-O_2/Ar (1:1) and reductive-H_2/Ar (1:1) environments, at a flow rate of 0.1 ml/min. The system was purged with argon between every alternating gas environment to ensure proper cleaning of the gas lines and the sample holder. To minimize the effects of electron beam such as contamination and sample damage, observations were made to determine the maximum electron beam dose the sample can withstand under each gaseous environment without damage. Hence, the electron dose rate was kept below 10^5 e nm^{-2} s^{-1}. Furthermore, the in-situ observation areas were not continuously exposed to the electron beam, in addition, areas outside the in-situ observation zones were systematically observed for comparison, to check for any significant artefacts caused by electron irradiation.

Results and Discussion

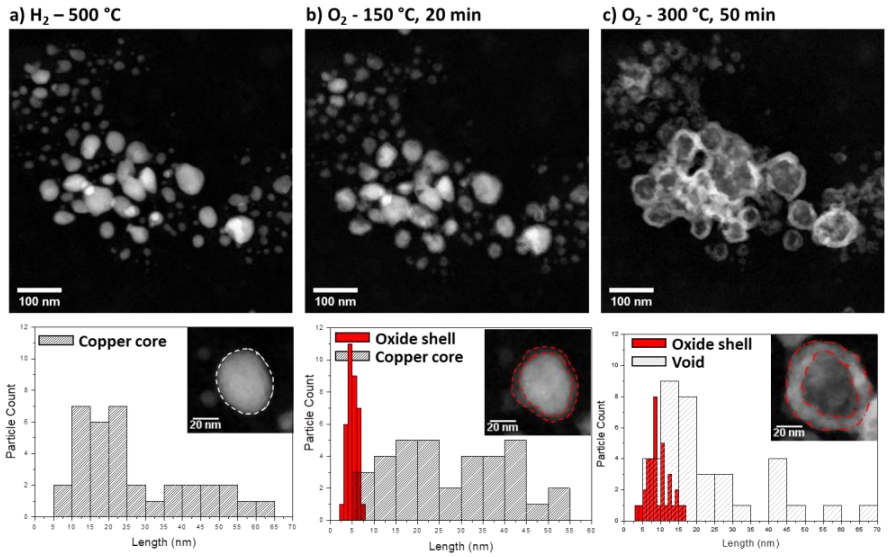

Figure 1: In-situ HAADF-STEM analyses with respective particle size distribution and oxide shell thickness from the same area of observation after 1 hour of reaction under, a) 0.5 atm H_2 partial pressure at 500 °C, b) 0.5 atm O_2 partial pressure at 150 °C and c) 0.5 atm O_2 partial pressure at 300 °C. Sample: Syn-1

Four experiments have been carried out on samples sputt1-3 and syn1 to assess the role of the nanoparticle size and reaction temperatures on the morphology and phase evolution of the NPs during the oxidation and reduction processes.

1. Oxidation as a function of temperature

1.1. NKE and Void Formation

Following the formation of copper nanoparticles (syn-1) at 500°C under H_2, the temperature was lowered down to 150 °C and oxygen at 0.5 atm partial pressure was introduced. At 150 °C, the initial stage of oxidation involves the formation of a thin layer of oxide on the surface of the Cu NPs (Figure 1). The oxide phase can be easily identified from the change in contrast on the STEM-HAADF images, resulting from the lower electron scattering intensity of the oxidized phase compared to the metallic phase due to the lowering of the local averaged atomic number as copper oxide is formed. At this temperature, only the presence of Cu_2O is reported in the literature [19,35]. With the augmentation of the temperature to 300 °C, three distinct morphologies can be distinguished with respect to the initial size of the metallic NPs (Figure 2a and Figure 2d).

The different NP morphologies are as follows:

(1) NPs with an initial size in the range of ~2 – 10 nm (Figure 2a, NP category-1) form compact oxide NPs after oxidation at 150 °C (Figure 2b).

(2) NP in the size range of ~10 – 25 nm (Figure 2a, NP category-2) form a central void Figure 2b) at the centre of an oxide rim. The hollow NPs eventually collapse upon increasing the temperature to 300 °C (Figure 2c).

(3) NPs with an initial diameter over 25 nm (Figure 2d, NP category-3) undergo the formation of a core@shell type morphology with a metallic copper core encapsulated by an oxide shell. Upon increasing the temperature from 150 °C to 300 °C at 5°C/min, these nanoparticles form hollow NPs (Figure 2e). After 30 min of oxidation at 300 °C, the presence of both Cu_2O and CuO phases is deduced from the analysis by Fast Fourier Transforms (FFT) of the STEM bright-field (BF) images (Figure S4a). After a prolonged flow of O_2, only the presence of the CuO phase is evidenced in Figure S4b, in agreement with the literature [15, 36].

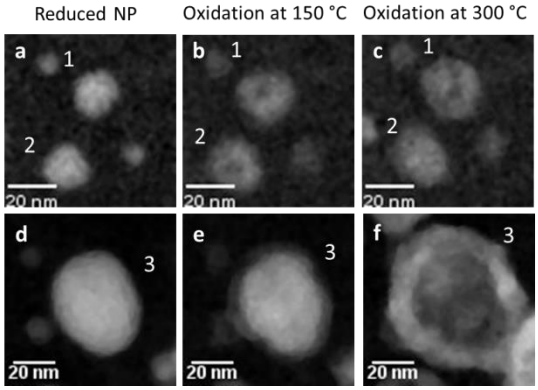

Figure 2: Illustration of size-dependent morphological transformation of cooper nanoparticles from the reduced state (a and d), after oxidation at 150 °C (b and e) and after oxidation at 300 °C (c and f). Numbers 1-3 represent the nanoparticle sets undergoing size-dependent shape evolution. Sample Syn-1

The smaller NPs (category-1, 2-10 nm) are expected to form compact oxide NPs in a shorter period due to the smaller distance of diffusion for copper and oxygen species [37]. Also, as the size of the NPs is very small, the number of nucleation sites on the particles is likely to be reduced, possibly leading to unidirectional oxide-phase growth [21,38]. On the contrary, for larger NPs, the nucleation frequency is expected to be higher, consequently favouring multiple nucleation points of the oxide phase on the surface of the metallic copper. Morphological evolution as a function of NP size and temperature of oxidation is consistent with the nano Kirkendall effect, wherein the deferential diffusion of Cu and O atoms results in outward growth of the oxide phase [14,23,26]. Above 8-10 nm diameter, the diffusion distance and the difference in diffusion coefficients between Cu and O atoms through bulk metallic Cu allow for the generation and aggregation of vacancies, leading to voids creation.

In addition to the size of the nanoparticles, an increase in temperature results in increased kinetics of oxidation as well as hollowing of the NPs. The time to complete the formation of hollow copper oxide for nanoparticles of an average initial diameter of ~40 nm and ~20 nm is plotted (Figure 3a) as a function of different constant temperature from 150 – 300 °C. The duration to form hollow oxide increases radically from ~2 hours at 150 °C to few seconds at 300 °C, for the same NPs size. The difference in the kinetics of hollowing stems from the temperature dependency of the diffusion coefficients of copper and oxygen atoms. Herein, we calculated the self-diffusion coefficient of copper as a function of temperature and size-dependent kinetics of hollowing at different temperatures using the reaction-diffusion model developed by Svoboda et al. [39]. The model estimates the duration to form hollow NPs by oxidation of metallic copper NPs in a gaseous environment where the diffusion coefficient of copper atoms in Cu_2O is much larger than that of the oxygen diffusion coefficient. The time to form hollow NPs from metallic Cu NPs according to Svoboda's equation is given by:

$$|\Delta$$

Where R is the ideal gas constant, T is the temperature of oxidation, R_0 is the initial radius (nm) of the nanoparticle, is the self-diffusion coefficient of Cu in Cu_2O and is the Gibbs energy of formation of the Cu_2O phase. The temperature-dependent Δg_{Cu_2O} is taken from the FactSage thermodynamic database [40]. Finally, A is a constant, taken from a range of values provided in the original paper. Here, a value of 0.07 is chosen based on the assumption that the diffusion coefficient of Cu in Cu (D) is significantly higher than and which in turn is larger than the value of the diffusion coefficient of O in Cu_2O (D).

Using the experimental data for nanoparticles of an average

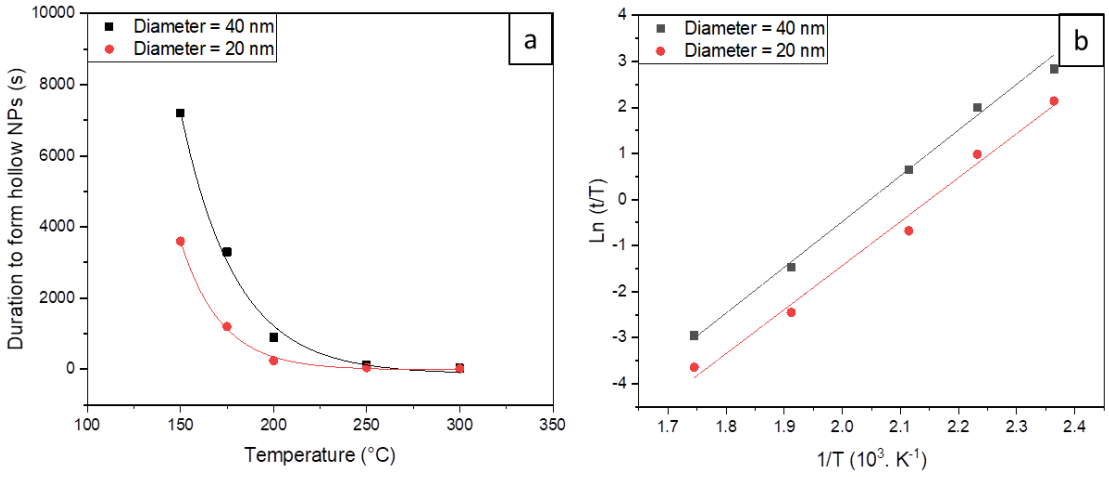

Figure 3: a) Experimental observation of hollow copper oxide nanoparticle formation during oxidation at constant temperature for 20 and 40 nm-sized Cu and b) linearized form of Arrhenius relation of self-diffusion coefficient of copper in Cu_2O, as a function of temperature.

diameter of ~40 nm and ~20 nm (Figure 3a), the diffusion coefficient of Cu in Cu_2O is estimated using the Svoboda model taking the experimental duration of complete oxidation into account, at a constant temperature. The temperature dependency of the diffusion coefficient of copper is modelled and plotted (Figure 3b) using the Arrhenius relation to determine the activation energy and pre-exponential coefficient of diffusion of copper:

————t, where is the pre-exponential diffusion coefficient, is the activation energy of diffusion (*R* and *T* carry the usual meaning). The activation energy and the pre-exponential coefficient are calculated to be 79 and 83 kJ/mol and 1.2× 10^{-8} and 3.6 × 10^{-9} cm²/s for 20 and 40 nm size particles, respectively. In comparison to the literature, the activation energy of copper self-diffusion reported here is in between that of Rice et al. (37.5 kJ/mol) for 5-10 nm size NPs and that in bulk copper (115 – 120 kJ/mol) (Figure S5) [14,41,42]. The extrapolated diffusion coefficient of Rice et al. (2.3 ×10^{-17} cm²/s) is an order of magnitude higher than in this study (3.7 ×10^{-18} cm²/s), at 150 °C [14]. Additionally, the predicted kinetics of hollow particle formation is comparatively slower than that of Rice et al. as shown in Figure S6. The slower diffusion coefficient and the transformation kinetics reported here may stem from the differences in the initial state of the particles and the experimental conditions. While the calculation of Rice et al. is based on the kinetics of chemical phase transition from metallic copper to copper oxide derived from in-situ UV-Vis analysis, we have considered the morphological transformation from an initial core@shell ($Cu@Cu_2O$) structure to a hollow NP (Cu_2O). UV-Vis spectroscopy tracks the bulk valence change of the NPs with the deduction of the precise time of oxidation completion. Instead, with STEM, the attainment of oxide layer stabilization is deduced from the imaging of the shell thickness. There is a probable time difference between the two techniques because the stabilization of the shell thickness may be delayed compared to the full oxidization i.e. the shell may continue to morphologically stabilize even after full oxidation, to attain surface energy minimisation through restructuring.

Furthermore, the presence of different defects concentrations (point, planer and volume defects) in individual NPs affects the kinetics as well as the intermediate morphological transformation during the NKE [43,44]. Hence, different diffusion regimes (surface, grain-boundary and/or bulk diffusion) are facilitated as a function of the nanoparticle microstructure and reaction condition [45]. In the current experiment, different intermediate states of nano-voids formations are noted. In some NPs, a single void is formed at the metal/metal oxide interface which then undergoes hollowing in a radially unidirectional manner (Figure 4a), in agreement with the report of Nilsson et al. [24]. Some NPs undergo multiple voids formation at the metal/metal oxide interface (Figure 4b), similar transformation has been observed by Nakamura et al [23]. In other NPs, three layers made of void@Cu@Cu_2O are observed (Figure 4c).

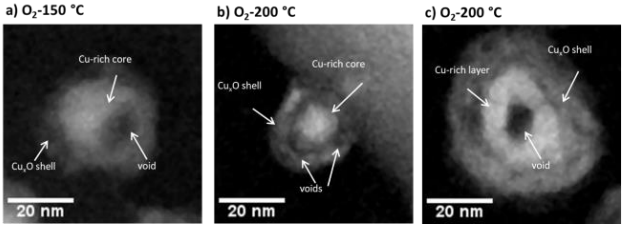

Figure 4: Intermediate stages of Kirkendall hollowing under 0.5 atm O_2 partial pressure, a) NP from Syn-1 at 150 °C, after 15 min – unidirectional hollowing, b) NP from Sputt-2 at 200 °C, after 20 min – multiple void formation and c) NP from Sputt-2 at 200 °C, after 20 min – evidence of void@Cu-rich@Cu_xO morphology.

The density of defects within the NPs plays a role in the kinetics of oxidation of Cu_2O which is highly dependent on neutral and singly charged copper vacancies [46]. In addition to the point defects, planar defects such as grain boundaries or twin boundaries are known to act as vacancy source and sink thus, affecting the void formation [44]. Similar to the present study, an in-situ liquid STEM study on the oxidation of bismuth NP revealed such intermediate nanostructures [43]. The authors reported three different intermediate structures leading to the central void formation in bismuth oxide NPs, seemingly stating the difference in the rate of diffusion of the reaction species due to different diffusion pathways facilitated by the presence of defects [43]. The kinetics of hollowing is a complex phenomenon and not only does it depend on the experimental/reaction conditions, but also largely varies from one NP to another within the same experimental setup.

1.2. Collapsing of the hollow nanoparticles

Upon increasing the temperature from 300 to 400 °C under 0.5 atm oxygen and after 20 min at 400°C, most hollow NPs have collapsed to form compact particles within the size range of 5-35 nm (sputtered samples), as shown in Figure 5. Under the same conditions, hollow NPs with an average diameter larger than 40 nm are still in the process of shrinking from their hollow nanostructures after 20 min. Moreover, different size-dependent intermediate states of transformation are observed after 20 min at 400 °C (Figure 5). From the difference in the HAADF contrast, segregation of copper species is noted at the interface between the hole and the oxide shell, as indicated by red arrows in Figure 5.

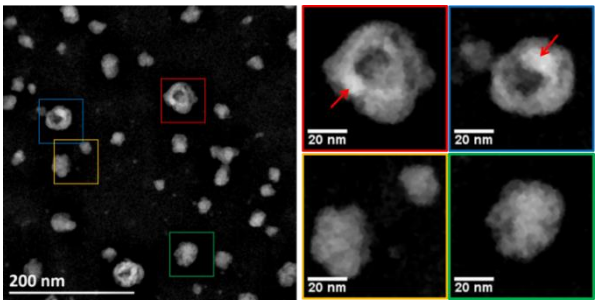

Figure 5: Evolution of the particles at 400 °C under 0.5 atm oxygen, after 20 min, showing the size-dependent intermediate state the hollow nanoparticles shrinkage. Sample: Sputt-2

Collapsing of the NPs is a consequence of surface energy minimization since compact nanoparticles are energetically favoured due to their lower surface energy in comparison to hollow nanospheres which are thermodynamically unstable [47,48]. The kinetics of shrinkage is affected by a number of parameters including the temperature of the reaction as well as the size of the NPs. [14,15,48,49]

The occurrence the shrinkage phenomena is evidenced by the in situ STEM data acquired at 400 °C (Figure 5). For larger NPs, below 400 °C, the duration to form compact NPs is significantly longer and above 500 °C the NPs tend to undergo sintering with the other NPs (Figure 9). Besides temperature, the initial size of the hollow NPs, the concentration of defects and the thermal history of the NPs impact the kinetics of shrinkage [49,50].

1.3. Faceting of nanoparticles

Faceting of the NPs becomes prominent when the NPs are either subjected to increasing temperature during oxidation or directly re-oxidized at 500 °C. In terms of phases, the presence of both Cu_2O and CuO is noticed at the beginning of the oxidation which eventually converts to CuO after prolonged exposure to oxygen.

The faceting of the copper oxide NPs is a contribution of surface atoms reorganisation since at 500 °C the NPs are above the Hüttig temperature of copper oxide (480 °C) which semi-empirically defines the temperature at which surface atoms start to exhibit significant mobility [51]. Thus atomic rearrangement on the surface of the NPs results in reconstruction and minimization of the surface energy of certain surface types. Additionally, adsorbed gas species can also induce surface reconstruction to stabilise certain facets [52].

To summarize, Figure 6 displays a schematic representation of the evolution of copper-based NPs in the size range of 30-40 nm as a function of incremental temperature for 1 hour at each temperature step, under O_2. At low temperature (50 - 150 °C), oxidation proceeds via the formation of a thin Cu_xO layer. At 300°C, voids are formed due to the oxide phase growth mechanism governed by the outward diffusion of copper atoms, which leads to the formation of hollow nanoshells composed of a mixture of Cu_2O and CuO. Upon prolonged oxidation at 300°C, Cu_2O is fully converted to CuO. A further increase in the temperature to 400°C results in the collapse of the hollow shells. Finally, at 500 °C and above, the copper oxide phase starts to form facetted NPs.

It should be noted that both NKE and hollow NP shrinkage are influenced by the duration of oxidation and the size distribution of the NPs. Therefore, the NPs can undergo void formation at a temperature as low as 50°C if either the NPs are dimensionally smaller or subjected to a longer oxidation

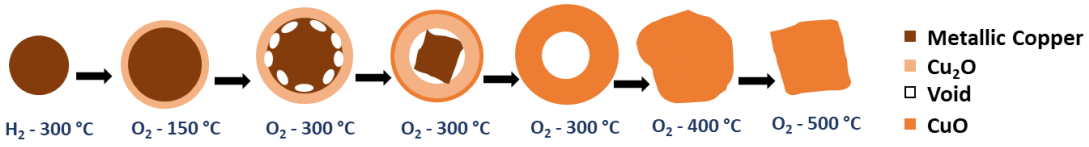

Figure 6: Schematic representation of the evolution of nanoparticle morphology as a function of the reaction temperature during oxidation of ~30-40 nm sized particles.

duration [14,19]. Similarly, shrinkage can occur at a lower temperature for smaller NPs or depending on the heating duration. Hence, the representation Figure 6 is a general overview and pathway of the shape changes occurring during the oxidation of copper NPs as a function of temperature.

2. Reduction of Copper Oxide Nanoparticles

Hydrogen at 0.5 atm partial pressure was introduced to copper oxide nanoparticles at different temperatures from 200°C to 500 °C and for different oxide phase morphologies, exhibiting either hollow or compact shapes. The gas was introduced at a constant temperature as well as at an increasing temperature.

The formation of metallic copper is very slow below 250 °C. Between 250 and 300 °C, the reduction of copper oxide results in metallic copper, as deduced from the change in HAADF contrast and the analysis of the FFT patterns of the HR images. Substantial changes can be noticed in the morphology in Figure 7, where images were taken from the same area of observation under different gas environments. Reduction leads to fragmentation of the particles as can be seen in several areas of the images. For instance, in the area highlighted by the red dotted circle, one hollow nanoparticle ends up forming three smaller nanoparticles after reduction in H_2. Moreover, the nanoparticles circled in blue are in the process of sintering under oxygen, followed by fragmentation under H_2 into one large nanoparticle (comparable in size to the initial metallic phase diameter of ~40 ± 5 nm) and eight smaller nanoparticles of ~2-6 nm. The fragmentation process is also illustrated by the size distribution histograms shown in Figure S7-S9. It is found that the NPs in the size range 0-10 nm are more numerous after re-reduction compared to the initial reduced sample.

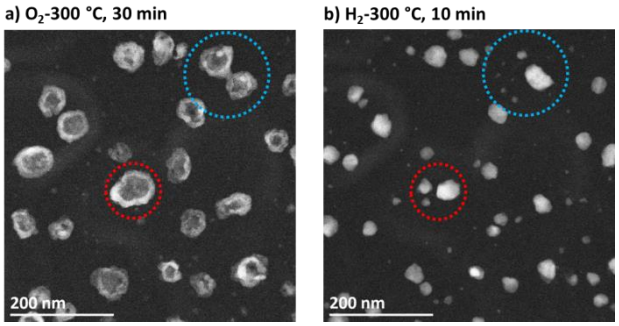

Figure 7: Fragmentation of hollow copper oxide nanoparticles at 300 °C upon reduction: a) copper oxide NPs under O_2 after 30 min and b) under H_2 after 10 min of gas flow. Sample: Sputt-1

The underlying phenomenon of fragmentation is visualised in real-time during the reduction reaction. The H_2 induced breakage of the particles into multiple fragmented NPs as a function of increasing temperature (from 150 °C to 300 °C) is presented in Figure 8, along with a schematic representation. Initially, the hydrogen molecules diffuse inside the hollow porous shell where the presence of defects promotes the reduction, thereby forming multiple reduction sites. The reduction sites can be deduced from the contrast of Figure 8. Once the reduction sites have been formed at around 220 °C (visualised from the difference in phase contrast), the metallic particles start to grow via particle migration and coalescence (PMC) mechanism with the neighbouring clusters. The process is very dynamic and stabilizes once the surface energy of the resulting particles is minimized.

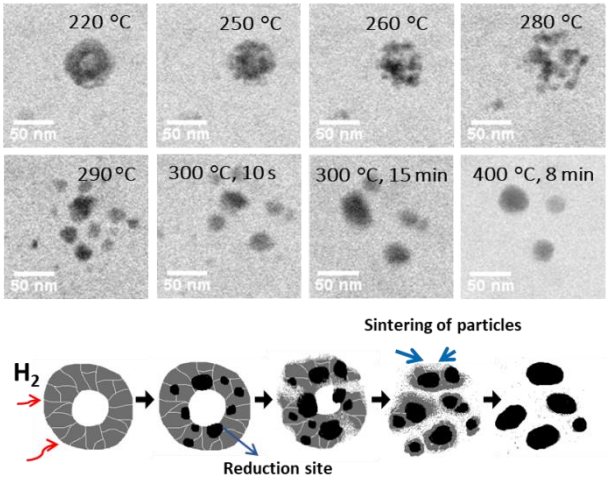

Figure 8: Reduction of hollow copper oxide nanoparticles under hydrogen heated from 150 °C to 300 °C at 5 °C/min rate, at 400 °C (top) and the schematic representation of fragmentation process with suggested mechanism (bottom). Sample: Synth-1.

The reduction of hollow CuO NPs has also been carried out at a constant temperature of 250 °C (Figure S10 – S12), which showed a similar fragmentation behaviour as discussed above.

At 400 °C, the reaction is too fast to observe any intermediate transformation step. Both collapsed (size below 40nm) and collapsing (above 40nm) CuO NPs are initially present, and form fragmented metallic copper particles within a few seconds of the introduction of the H_2 gas (Figure S13). With longer exposure to high temperature under H_2, the NPs tend to grow into larger particles (Figure S14) and the process of fragmentation is evidenced only in few areas. This could be explained by the high rate of PMC induced by the temperature. In other words, the reduction mechanism at 400

°C is likely similar to that at 300 °C, but due to increased temperature, the dynamics of the fragmentation and the subsequent growth process are faster.

The reduction of fully compact shaped NPs at 250°C (Figure S15) also produces fragmented nanoparticles. This observation contradicts the speculation of Weststrate et al. who have suggested the presence of Kirkendall void as a prerequisite for the fragmentation of cobalt-based NPs [53]. Based on our observations, it can be concluded that the oxide NPs (copper) undergo fragmentation regardless of the shape of the particles (hollow and compact morphologies).

The origin of reduction-fragmentation is visualised under different temperatures and nanoparticle morphologies could arise from a combination of unit cell volume shrinkage, nucleation and growth phenomena [26,27,53]. The unit cell accounts for 60 % shrinkage in volume during the transformation of CuO to metallic Cu. In terms of nucleation and growth, the genesis of numerous nucleation sites is more likely to produce multiple individual metallic particles as opposed to the growth of an already reduced domain, observed from the difference between the present study and the literature [21]. At higher H_2 pressure, the formation of multiple nucleation sites was observed, followed by growth, to form individual NPs. In contrast at lower H_2 partial pressure, growth of metallic copper phase occurred in a layer by layer fashion from an initial nucleation site formed on the Cu_2O surface [21].

3. Shape, sintering and evaporation of the copper nanoparticles

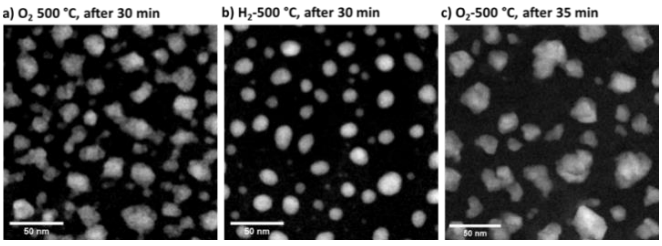

Figure 9: Reduction and re-oxidation of copper oxide nanoparticles at 500 °C: a) under O_2 after 30 min of gas flow b) under H_2 after 30 min of gas flow and c) NPs after re-oxidation after 35 min of oxidation. The images are not from the same area of observation. Sample: Sputt-3

At 500 °C, the shapes of copper-based nanoparticles are drastically different depending on whether they are composed of metallic phase under hydrogen (Figure 9b) or copper oxide under O_2 (Figure 9a, c). The compact facetted oxide nanoparticles exhibit spherical morphology after reduction, with some of the NPs forming truncated octahedron-like shapes. From the HR-STEM image, the (111) and (200) facets of copper have been identified. After re-oxidation at the same temperature, the oxide NPs undergo faceting with major (111) and (-111) surfaces exposed. Similar gas-induced NP morphology evolution has been observed in other transition metal-based nanoparticles [54–57].

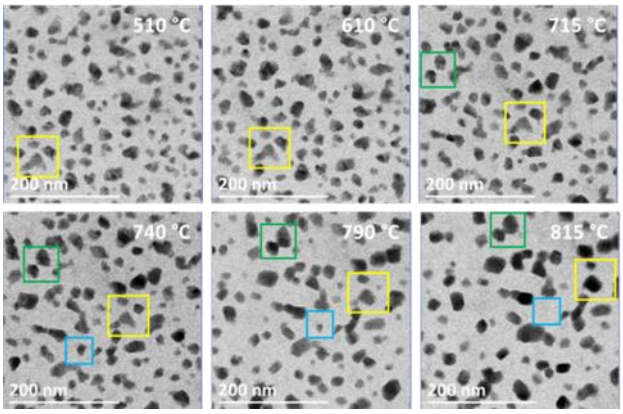

Figure 10: Sintering behaviour of copper oxide NPs, heat treatment from 500 °C to 815 °C at 1 °C/s. The coloured squares illustrate the different growth mechanisms of the NPs. Sample: Sputt-2

Upon increasing the temperature from 400 to 900 °C at 1°C/s, the NPs are subjected to different growth mechanisms, namely particle migration and coalescence (PMC), Ostwald ripening (OR) and coalescence via bridge formation, as a function of gas atmosphere (O_2 and H_2). Under O_2, OR is the dominant growth mechanism as visualised from the growth of the particles in the yellow squares in Figure 10 at the expense of the smaller NPs in blue squares in Figure 10. The growth of the NPs is either visualised through an increase in the apparent size of the NPs or through the increase in the thickness-dependent contrast. In some areas, the NPs grow via surface reconstruction to form bridges between the NPs, indicated by the green squares in Figure 10. This type of growth is also observed at a lower temperature for NPs undergoing hollowing (blue dotted circle in Figure 7a). The process of bridging and eventual sintering of the nanoparticles have been termed as attractive migration and coalescence by Yang et al [58]. Attractive migration and coalescence differ from that of PMC since the particles do not experience Brownian-like motion and the underlying mechanism is similar to that of OR, involving atomic migration [59]. For this growth mechanism, the

distance between the NPs as well as the wetting behaviour of the NPs are deemed to be important. Compared to metallic copper, copper oxide exhibits increased wetting behaviour due to stronger adhesion between the NPs and the support [60]. The resulting spreading of the oxide NPs and proximity to the neighbouring NPs promotes atomic migration and eventual coalescence [61].

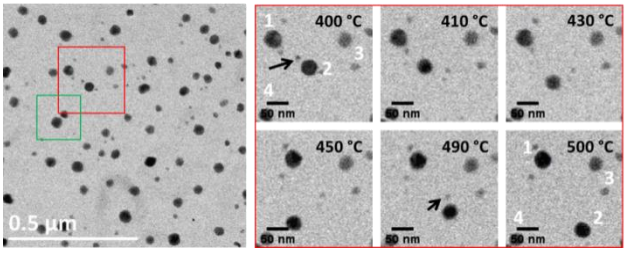

Figure 11: BF image extracted from a video with red and green squares depicting PMC and coalescence via bridging, respectively (left) and series of images presenting PMC during in-situ heating from 400 to 900 °C, 1 °C/s under H_2. The snapshots are taken at 400 °C (0 s), 410 °C (10 s), 430 °C (30 s), 450 °C (50 s), 490 °C (90s) and 500 °C (100 s).

Under H_2, the metallic copper NPs undergo temperature-dependent growth mechanism as identified by red and green squares in Figure 11. The red square shows the area where PMC is noticed between 400 and 500 °C. The snapshots of the video depict the dynamic movement of the nanoparticles captured in real-time until the temperature reached 500 °C. Particles 3 and 4 remain fixed in their position while particles 1 and 2 undergo hopping movement. The distance moved by particle 1 is negligible but Brownian-like motion is particularly discernible for particle 2. Besides, the very small particles marked by black arrows are merged to particle 2 via coalescence. Interestingly, particle number 2 does not experience any more hopping motion once the temperature reaches 500 °C.

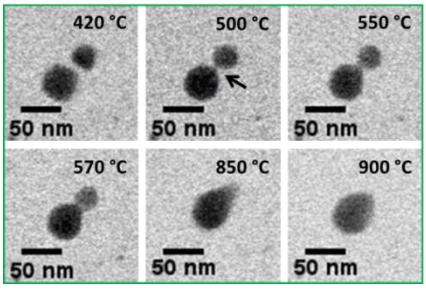

Figure 12: Particles undergoing attractive migration and coalescence as observed during in-situ heating from 400 to 900 °C, 1 °C/s under H_2. The snapshots are taken at 420 °C (20s), 500 °C, (100 s), 550 °C (150 s), 570 °C (170 s), 850 °C (350 s) and 900 °C (400 s).

The green square in Figure 11 depicts the coalescence of the NPs via bridging at a temperature of 500 °C and above. The emergence of the bridge and the progressive sintering are presented in a series of images from 420 to 900 °C in Figure 12. Martin et al. have studied the sintering of metallic copper at low H_2 partial pressure (9×10^{-5} atm) and under vacuum [12]. They state that at 500 °C under H_2, the NPs undergo growth via atomic migration (OR) while under vacuum, the size of the NPs stays constant for the same annealing duration. No other sintering mechanism such as PMC or coalescence via bridging has been reported in their study, hence highlighting the importance of partial pressure on nanoparticles behaviour.

As a consequence, several factors including metal-support interactions, NPs size and distribution across the substrate and gas partial pressure determine the mechanisms of sintering.

The last aim of this study was to understand the oxidation-reduction behaviour of copper NPs at operating conditions close to those of CLC, i.e .between 800 and 1000 °C. However, it is difficult to stabilise the NPs in the in-situ STEM setup above 700 °C. Depending on the duration of thermal treatment and the initial size of the NPs, starting at 700 °C, the NPs undergo slow depletion in size until all the NPs are evaporated from the substrate. The rate of evaporation is even faster at 900 °C - taking only a few minutes for 10 – 30 nm-sized NPs to evaporate (Figure S17). The effect of different gas atmospheres on the evaporation kinetics could not be discerned from the current experiments since the rate of evaporation is very fast and the kinetics is influenced by other factors such as NPs size, shape and the physical properties of the substrate. Size-dependent melting temperature depression and eventual evaporation either via liquid phase or direct sublimation have been reported previously for similar NP systems during in-situ STEM observation [62–64].

Conclusions

In-situ analysis by transmission electron microscopy of the oxidation/reduction reactions at different temperatures were carried out on chemically synthesized and sputtered copper nanoparticles to understand the changes in the morphology of the NPs. At a low temperature, with the introduction of an oxidative environment, a thin layer of oxide is formed

surrounding the metallic core that eventually turns into a hollow particle upon increasing the temperature. Further augmentation of the temperature leads to collapsing of the hollow nanoparticles with subsequent faceting of the NPs. The reduction of the hollow nanoparticles results in fragmentation into smaller particles. The process of fragmentation is very dynamic and stabilizes once the surface energy of the resulting particles is minimized.

The shape evolution of the NPs during oxidation and reduction are subjected to various parameters including NP initial size and density of structural defects, temperature, pressure and duration of the gas exposure. Furthermore, depending on the temperature and the gas atmosphere, different sintering mechanisms are activated. The underlying phenomena concerning the different morphological changes and the growth mechanisms illustrated throughout this study originate from the migration of the copper phase and are connected by the minimization of the energy of the global system.

In this work, the significance of in-situ STEM under relevant industrial reaction condition (particularly, higher gas pressure) is demonstrated in comparison to previous studies conducted at lower partial pressure. Nevertheless, we have also highlighted some challenges faced during the experiments, for instance, the difficulties to monitor some of the intermediate changes during the reaction when the reaction kinetics is very fast, and more importantly, the evaporation of the copper phase during high-temperature reaction. The confinement of the nanoparticles remains a challenge to characterize such systems at very high operating temperature, using in-situ STEM.

Author Contributions

S.S., M.B, and C.B carried out the experiments. S.S. interpreted the data and wrote the manuscript. A.L., A-S.G, D.C and O.E conceived the original idea. A.L., A-S.G and D.C supervised the project. O.E. directed the project. All authors contributed to the interpretation of the results, critical feedback, analysis and editing of the manuscript.

Conflicts of interest

There are no conflicts of interests to declare.

Acknowledgements

S Sharna thankfully acknowledges IFP Energies Nouvelles for funding this work.

We are grateful to Manuel Acosta (IPCMS) for the sputtered copper samples.

Notes and references

1 W-H. Xu, L. Wang, Z. Guo, X. Chen, J. Liu and X-J. Huang, *ACS nano*, 2015, **9**, 241–250.
2 P. Shen, Y. Liu, Y. Long, L. Shen and B. King, *The journal of physical chemistry. C, Nanomaterials and interfaces*, 2016, **120**, 8900–8906.
3 Y. Gao, F. P. Cao, X. Lei, L. Mang, S. Cheng and J. Song, *Nanoscale*, 2016, 4852–4863.
4 M. B. Gawande, A. Goswami, F-X. Felpin, T. Asefa, X. Huang, R. Silva, X. Zou, R. Zboril and R. S. Verma, *Chemical reviews*, 2016, **116**, 3722–3811.
5 C. Ratnasamy and J. P. Wagner, *Catalysis Reviews*, 2009, **51**, 325–440.
6 K. C. Waugh, *Catalysis Today*, 1992, **15**, 51–75.
7 T-J. Huang and D-H.Tsai, *Catalysis Letters*, 2003, **87**.
8 M. Ozawa, H. Toda, O. Kato and S. Suzuki, *Applied Catalysis B: Environmental*, 1996, **8**, 123–140.
9 J. Adanez, A. Abad, F. Garcia-Labiano, P. Gayan and L. F. De Diego, *Progress in Energy and Combustion Science*, 2012, **38**, 215–282.
10 A. Lambert, A. Tilland, W. Pelletant, S. Bertholin, F. Moreau, I. Clemençon and M. Yazdanpanah, *FUEL*, 2018, **216**, 71–82.
11 X. He, Y. Wang, W. Zhang, M. Dong, G. Wang, B. Zhang, Y. Niu, S Yao, X. He and H. Liu, *ACS Catalysis*, 2019, **9**, 2213–2221.
12 T. E. Martin, P. L. Gai, and E. D. Boyes, *ChemCatChem*, 2015, **7**, 3705–3711.
13 M. D. Susman, Y. Feldman, T. A. Bendikov, A. Vaskevich and I. Rubinstein, *Nanoscale*, 2017, **9**, 12573–12589.
14 K. P. Rice, A. S. Paterson and M.P Stoykovich, *Particle & Particle Systems Characterization*, 2015, **32**, 373–380.
15 R. Nakamura, D. Tokozakura, J. G. Lee, Mori and H. Nakajima, *Acta Materialia*, 2008, **56**, 5276–5284.
16 M. Mansoor, L. Favergeon and M. Pijolat, *Thermochimica Acta*, 2013, **570**, 41–50.
17 Q. Zhu, L. Zou, G. Zhou, W. A. Saidi and Y. C. Judith, *Surface Science*, 2016, **652**, 98–113.
18 R. Nakamura, D. Tokozakura, J. G. Lee, H. Mori, H. Nakajima, *Material Science Forum*, 2007, **561-565**, 1703–1706.
19 D. Tokozakura, R. Nakamura, H. Nakajima, J. G. Lee and H. Mori, *Journal of Material Research*, 2007, **22**, 2930–2935.
20 A. Yabuki and S. Tanaka, *Materials Research Bulletin*, 2011, **46**, 2323–2327.
21 A. P. LaGrow, M. R. Ward, D. C. Lloyd, P. L Gai, E. D. Boyes, *Journal of the American Chemical Society*, 2017, **139**, 179–185.
22 R. Nakamura, G. Matsubayashi, H. Tsuchiya, S. Fujimoto, H. Nakajima, *Acta Materialia*, 2009, **57**, 4261–4266.
23 R. Nakamura, D. Tokozakura, H. Nakajima, J-G Lee, H. Mori, *Journal of Applied Physics*, 2007, **101**, 74303.
24 S. Nilsson, D. Albinsson, T. J. Antosiewicz, J. Fritzsche and C. Langhammer, *Nanoscale*, 2019, **11**, 20725–20733.

25 P. Haugsrud and P Kofstad, *Material Science Forum*, 1997, **251-254**, 65–72.
26 A. P. LaGrow, D. C. Lloyd, P. L. Gai and E. D. Boyes, *Chem. Mater.*, 2017, **30**, 197–203.
27 S. Sadasivan, R. M. Bellabarba and R. P. Tooze, *Nanoscale*, 2013, **5**, 11139–11146.
28 J. Y. Kim, J. A. Rodriguez, J. C. Hanson, A. I. Frenkel and P. L. Lee, *Journal of the American Chemical Society*, 2003, **125**, 10684–10692.
29 J. A. Rodriguez, J. Y. Kim, J.C. Hanson, M. Perez and A. I. Frenkel, *Catalysis Letters*, 2003, **85**, 247–254.
30 S. Carenco, C. Boissière, L. Nicole, C. Sancez, P. Le Floch and N. Mézailles, *Chem. Mater.*, 2010, **22**, 1340–1349.
31 K. Dembélé, PhD, University of Strasbourg, 2017.
32 Protochips, Protochip Atmosphere, https://www.protochips.com/products/atmosphere/.
33 L. F. Allard, W. C. Bigelow, M. Jose-Yacaman, D. P. Nackashi, J. Damiano, S. E. Mick, *Microscopy research and technique*, 2009, **72**, 208–215.
34 L. Allard, S. Overbury, W.C. Bigelow, M. Katz, D. Nackashi and J. Damiano, *Microscopy and Microanalysis*, 2012, **18**, 208–215.
35 R. Nakamura, J. G. Lee, D. Tokozakura, H. Mori and H. Nakajima, *Materials Letters*, 2007, **61**, 1060–1063.
36 Li J, Vizkelethy G, Revesz P, Mayer JW and Tu KN, *Journal of Applied Physics*, 1991, **69**.
37 G. J. Cheng and A. R. H. Walker, *Anal Bioanal Chem*, 2010, **397**, 1057–1069.
38 L. Favergeon, M. Pijolat and M. Soustelle, *Thermochimica Acta*, 2017, **654**, 18–27.
39 J. Svoboda, F.D. Fischer and D. Vollath, *Acta Materialia*, 2009, **57**, 1912–1919.
40 C.W. Bale, P. Chartrand, S.A. Decterov, G. Eriksson, K. Hack, R. Ben Mahfoud, J. Melançon, A.D. Pelton and S. Petersen, FactSage thermochemical software and databases, *CALPHAD Journal*, 2002, **62**, 189–228.
41 N. L. Peterson and C. L. Wiley, *Journal of Physical Chemistry Solids*, 1984, **45**, 281–294.
42 R. Haugsrudz and T. Norby, *Journal of Electrochemical Society*, 1999, **146**, 999–1004.
43 K-Y. Niu, J. Park, H. Zheng and A. P. Alivisatos, *Nano letters*, 2013, **13**, 5715–5719.
44 C-L. Huang, W-L Weng, C-N. Liao and K. N. Tu, *Nature Communications*, 2018, 340.
45 H. J. Fan, M. Knez, R. Scholz, D. Hesse, K. Nielsch, M. Zacharias, and U. Gösele, *Nano letters*, 2007, **7**, 993–997.
46 E. A. Goldsteina, T. M. Gür, R. E. Mitchell, *Corrosion Science*, 2015, **99**, 53–65.
47 A.V. Evteev E.V. Levchenko I.V. Belova & G.E. Murch, *Philosophical Magazine*, 2008, 1525–1541.
48 A. M. Gusak T. V. Zaporozhets K. N. Tu & U. G, *Philosophical Magazine*, 2007, 4445–4464.
49 A. M. Gusak and K. N. Tu, *Acta Materialia*, 2009, **57**, 3367–3373.
50 K. N. Tu and U. Gösele, *Applied Physics Letters*, 2005, **86**, 093111.
51 Y. Dai, P. Lu, Z. Cao, C. T. Campbell and Y. Xia, *Chem Soc Rev*, 2018, **47**, 4314_4331.
52 F. Tao and P. A. Crozier, *Chemical reviews*, 2016, **116**, 3487–3539.
53 C. J. Weststrate, M. M. Hauman, D. J. Moodley, A. M. Saib, E. van Steen and J. W. Niemantsverdriet, *Top. Catalysis*, 2011, **54**, 811–816.
54 T. Uchiyama, H. Yoshida, Y. Kuwauchi, S. Ichikawa, S. Shimada, M. Haruta, and S. Takeda, *Angewandte Chemie*, 2011, **50**, 10157–10160.
55 H. Mistry, F. Behafarid, S. R. Bare, and B. R. Cuenya, *ChemCatChem*, 2014, **6**, 348–352.
56 P. L. Hansen, J. B. Wagner, S. Helveg, J. R. Rostrup-Nielsen, B. S. Clausen, H. Topsoe, *Science*, 2002, **295**, 2053–2055.
57 C. Dessal, A. Sangnier, C. Chizallet, C. Dujardin, F. Morfin, J-L. Rousset, M. Aouine, M. Bugnet, P. Afanasiev and L. Piccolo, *Nanoscale*, 2019, **11**, 6897–6904.
58 W.C. Yang, M. Zeman, H. Ade, R.J. Nemanich, *Physical review letters*, 2003, **90**.
59 A. T. Delariva, T. W. Hansen, S. R. Challa and A. K. Datye, *Journal of Catalysis*, 2013, **308**, 291–305.
60 P. L. Gai, B. C. Smith and G. Owen, *Nature*, 1990, **348**, 430–432.
61 J.-X. L. a. W.-X. Li R. Ouyang, *Journal of the American Chemical Society*, 2013, **135**, 1760–1771.
62 M. A. Asoro, D. Kovar and P. J. Ferreira, *ACS nano*, 2013, **7**, 7844–7852.
63 J. Li, Z. Wang, Y. Li and F. L. Deepak, *Advanced science*, 2019, **6**, 1802131.
64 A. Chmielewski, J. Nelayah, H. Amara, J. Creuze, D. Alloyeau, G. Wang and C. Ricolleau, *Physical review letters*, 2018, **120**, 25901.